nature photonics

Article

https://doi.org/10.1038/s41566-024-01446-7

Delivering broadband light deep inside diffusive media

Received: 24 September 2023

Accepted: 16 April 2024

Published online: 23 May 2024

Check for updates

Rohin McIntosh [1], Arthur Goetschy [2], Nicholas Bender [3], Alexey Yamilov [4], Chia Wei Hsu [5], Hasan Yılmaz [6] & Hui Cao [7]

Wavefront shaping enables the targeted delivery of coherent light into random-scattering media, such as biological tissue, by the constructive interference of scattered waves. However, broadband waves have short coherence times, weakening the interference effect. Here we introduce a broadband deposition matrix that identifies a single input wavefront that maximizes the broadband energy delivered to an extended target deep inside a diffusive system. We experimentally demonstrate that long-range spatial and spectral correlations result in sixfold energy enhancement for targets containing 1,700 speckle grains and located at a depth of up to ten transport mean free paths, even when the coherence time is an order of magnitude shorter than the diffusion dwell time of light in the scattering sample. In the broadband (fast decoherence) limit, enhancement of energy delivery to extended targets becomes nearly independent of the target depth and dissipation. Our experiments, numerical simulations and analytic theory establish the fundamental limit for broadband energy delivery deep into a diffusive system, which has important consequences for practical applications.

Waves propagate diffusively through disordered media, such as biological tissue, clouds and paint, due to random scattering. This process is deterministic for elastic scattering in static disordered structures, enabling the control of wave propagation by input wavefront shaping[1–3]. For a coherent beam, spatial modulation of its wavefront incident on a random medium can manipulate the interference of scattered waves from different paths, resulting in light focusing[4–10], enhancement of total transmission[11–21] or energy deposition deep inside scattering media[7,22–40]. Such success relies on the coherence time τ_c of the input light exceeding the diffusion dwell time τ_d of light inside the multiple-scattering system, enabling scattered waves to remain phase coherent and thereby interfere. However, many applications use partially coherent light, for example, broadband light from a supercontinuum source or a superluminescent diode. Once $\tau_c < \tau_d$, dephasing among the scattered waves will weaken their interference, diminishing the power of wavefront shaping. Previous studies have shown that the focusing efficiency decreases for broadband light, as the coherence time τ_c is inversely proportional to the spectral bandwidth $\Delta\omega$ (refs. 41–45). Furthermore, the focal targets in various applications, such as detectors for communications and cells or tissues for photothermal therapy or laser microsurgery, contain many wavelength-scale speckles. Simultaneously enhancing the intensities of all of the speckles within the target by shaping a single wavefront is more difficult than focusing on a single speckle[19]. Having to contend with both temporal decoherence and spatial decorrelation, broadband deposition to a large target is substantially more challenging than narrowband focusing on a wavelength-scale target.

Our aim is to deliver broadband light of $\tau_c \ll \tau_d$ to an extended target with dimensions much greater than λ at a depth well exceeding the transport mean free path ℓ_t in a diffusive system. Although

[1]Department of Physics, Yale University, New Haven, CT, USA. [2]Institut Langevin, ESPCI Paris, PSL University, CNRS, Paris, France. [3]School of Applied and Engineering Physics, Cornell University, Ithaca, NY, USA. [4]Physics Department, Missouri University of Science & Technology, Rolla, MO, USA. [5]Ming Hsieh Department of Electrical and Computer Engineering, University of Southern California, Los Angeles, CA, USA. [6]Institute of Materials Science and Nanotechnology, National Nanotechnology Research Center (UNAM), Bilkent University, Ankara, Turkey. [7]Department of Applied Physics, Yale University, New Haven, CT, USA. e-mail: hui.cao@yale.edu

https://doi.org/10.1038/s41566-024-01446-7

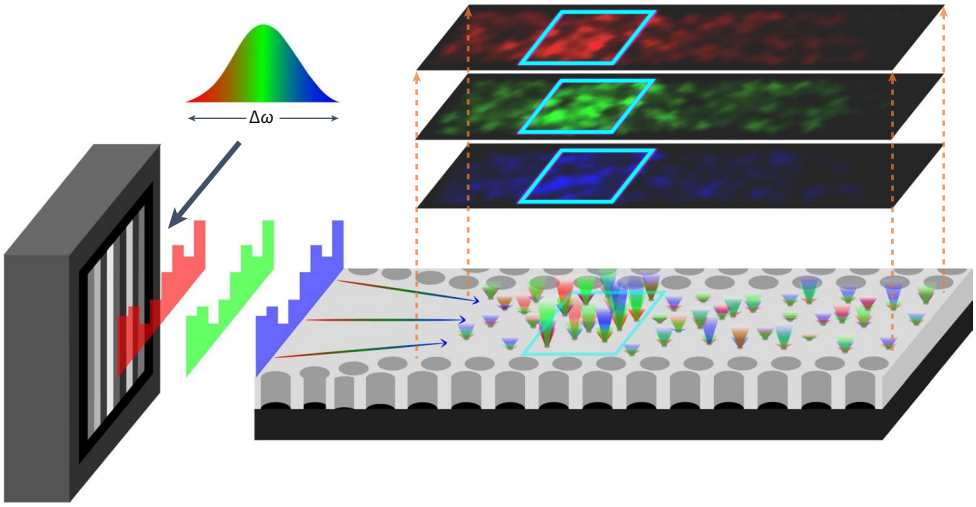

Fig. 1 | Illustration of the experimental platform. Broadband light is modulated by an SLM and delivered to an extended target (cyan box) inside a planar waveguide with randomly distributed scatterers. A tapered waveguide segment directs light into the disordered region with length $L = 50$ μm and width $W = 15$ μm. The transport mean free path is $\ell_t = 3.3$ μm. A small fraction of the light is scattered out of the plane, allowing an interferometric measurement of field distribution inside the waveguide. The broadband deposition matrix is experimentally constructed from the frequency-resolved matrix that maps the incident wavefront to the field distribution within the target. Its eigenvector with the largest eigenvalue gives a single spatial wavefront that simultaneously enhances the energy in the target for all of the frequencies within the input light, as exemplified by three images of intensity distributions at different frequencies.

short-range correlations of scattered waves dictate light focusing to a wavelength-scale target, long-range spatial correlations play an essential role in delivering light to a large target[19]. It has been theoretically shown that non-local spectral correlations facilitate the broadband enhancement of total transmission by wavefront shaping[46]. For energy delivery deep into a turbid medium[40], however, the capabilities of wavefront shaping for broadband energy enhancement and their underlying physics are not known. Open questions include the following. Is it possible to deterministically find a single wavefront that maximizes broadband energy delivery to an extended target deep inside a diffusive system? What is the fundamental limit for the delivered energy and how does it depend on the target depth and input bandwidth?

To address these questions, we introduce the broadband deposition matrix $\mathcal{A}$, whose eigenvector with the largest eigenvalue gives the input wavefront that maximizes the energy (summed over all of the input frequencies) delivered to a target of arbitrary size and shape. This approach always finds the global maximum—the highest possible energy. A schematic of our experimental platform is illustrated in Fig. 1, depicting a single input wavefront that optimizes energy delivery for multiple frequencies. Even when the coherence time of an input light is ten times shorter than the dwell time of diffusive waves in the disordered medium, we observe a sixfold enhancement of total energy (spatially and temporally integrated intensity) in a large target that contains approximately 1,700 speckles at a depth of $9\ell_t$. The long-range spectral correlations greatly slow down the drop of energy enhancement with increasing bandwidth (decreasing coherence time τ_c). In addition, unlike the broadband enhancement of tight focusing (to a wavelength-scale target) that rapidly decays with the depth, the broadband energy enhancement over a large target increases slightly with the depth, and becomes nearly depth invariant when $\tau_c \ll \tau_d$. These results can be explained by the distinct depth dependence of short-range correlations for the wavelength-scale target and long-range correlations for the extended target. The sustainability of energy enhancement for broad bandwidths and large areas at any depth illustrates that long-range spatial and spectral correlations are vital for energy delivery deep into diffusive media by wavefront shaping.

A further question is how light absorption or dissipation in multiple-scattering samples affects the efficiency of wavefront shaping. Previous studies show that optical dissipation in random media profoundly impacts the coherent control of wave transport[47–50]. The dissipation strength in a diffusive medium can be described by the dissipation time τ_a. We find that once the coherence time of the input light τ_c becomes shorter than τ_a, the dissipation effects on the large-area energy enhancement diminish, as the decoherence effect overwhelms the dissipation effect. More specifically, the decoherence of scattered waves becomes more detrimental to the interference effect than the attenuation of long scattering paths by dissipation. This conclusion is supported by our numerical simulations and analytic theory.

We note that all the results from this study are generalizable to the linear scattering of any waves, including acoustic and electron waves. The broadband deposition matrix introduced here provides the fundamental physical limit for single-wavefront energy delivery into diffusive media for any input bandwidth, target area and deposition depth, giving a general upper bound with which to constrain wavefront optimization.

Results

Broadband deposition matrix

Monochromatic energy deposition can be described by the deposition matrix $\mathcal{Z}(\omega_0)$ that maps incident wavefronts at frequency ω_0 to internal electric fields in a target of arbitrary shape and size[40]. The deposition matrix generalizes the concept of reflection and transmission matrices to the interior of a scattering medium, approaching those matrices at the medium entrance and exit, respectively. The eigenvector of $\mathcal{Z}^\dagger(\omega_0)\mathcal{Z}(\omega_0)$with the largest eigenvalue gives the incident wavefront of monochromatic light that deposits maximum energy (spatially integrated intensity at ω_0) in the target region. As the frequency of input light ω is detuned from ω_0, the energy deposited by the monochromatic eigenvector (of ω_0) decreases rapidly, approaching that of random wavefront illuminations. The full-width at half-maximum $\delta\omega$ of this decay curve is inversely proportional to the dwell time of light τ_d (ref. 46). Deeper into a diffusive system, τ_d is longer and $\delta\omega$ becomes narrower.

For broadband deposition, we consider an input light of frequency bandwidth $\Delta\omega$. The nominal number of uncorrelated spectral channels is $M = \Delta\omega/\delta\omega + 1$. Each spectral channel requires a distinct wavefront for maximum energy delivery to the same target. To find a single wavefront

https://doi.org/10.1038/s41566-024-01446-7

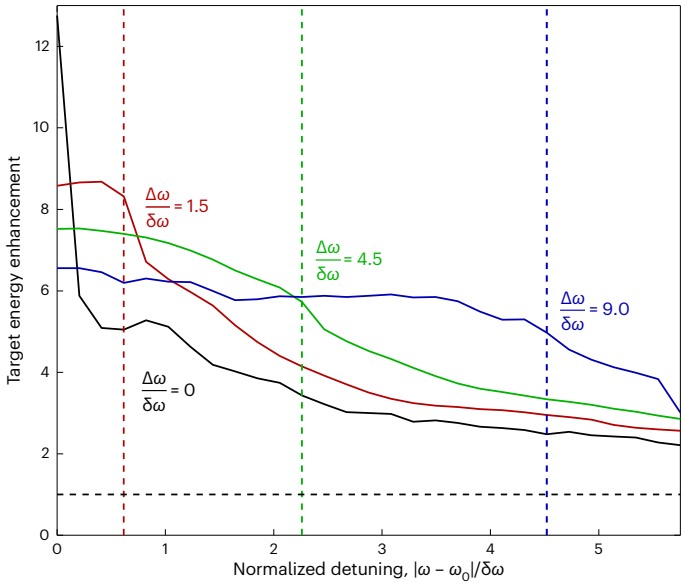

Fig. 2 | Targeted broadband energy delivery. Frequency-resolved energy enhancement over a random input wavefront, in a 10 × 10 μm² target region centred at depth $z = 30$ μm in the disordered waveguide, for the maximum deposition eigenchannel with centre frequency ω_0 and bandwidth $\Delta\omega$. Both frequency detuning $|\omega - \omega_0|$ and input bandwidth $\Delta\omega$ are normalized by the spectral correlation width $\delta\omega$ at this depth. The normalized bandwidths are $\Delta\omega/\delta\omega = 0$ (black), 1.5 (red), 4.5 (green), 9.0 (blue). The experimental results are averaged over ω_0 within the wavelength range of 1,551–1,556 nm and over two disorder realizations.

that maximizes energy delivery over the entire bandwidth of $\Delta\omega > \delta\omega$, we introduce the following broadband deposition matrix:

$$\mathcal{A}(\Delta\omega) = \int_{\Delta\omega} \mathrm{d}\omega\, I(\omega)\, \mathcal{Z}^{\dagger}(\omega)\mathcal{Z}(\omega), \qquad (1)$$

where $I(\omega)$ is the spectral intensity of input light, normalized to $\int_{\Delta\omega}\mathrm{d}\omega I(\omega) = 1$. The eigenvector of $\mathcal{A}(\Delta\omega)$ with the largest eigenvalue represents the single wavefront that maximizes the energy deposition over the spectral bandwidth $\Delta\omega$ in a given target region. The corresponding eigenvalue is the maximum energy (spectrally integrated intensity over $\Delta\omega$) on the target.

Experimentally, we study broadband optical energy delivery into a diffuse waveguide (Fig. 1). The planar waveguides are fabricated on a silicon-on-insulator wafer with reflective photonic-crystal sidewalls to confine light. Randomly arranged air holes with a diameter of $d = 100$ nm are etched into the silicon layer to serve as scatterers, and the transport mean free path is $\ell_t = 3.3$ μm (ref. 51). The disordered segment has a length of $L = 50$ μm and a width of $W = 15$ μm, supporting $N = 55$ guided modes in the probed wavelength range of 1,551–1,556 nm in our experiment. Monochromatic light from a tunable infrared laser is shaped by a spatial light modulator (SLM) and then coupled into the silicon waveguide. Since $L \gg \ell_t$, light undergoes multiple scattering as it traverses the disordered region of the waveguide. A small amount of light is scattered out of the plane, enabling the direct probing of field distribution inside the waveguide in an interferometric measurement (Methods).

We consider a target area with dimensions of 10 × 10 μm² centred at a depth of 30 μm. The input wavelength λ is scanned from 1,551.0 to 1,556.0 nm with a step size of 0.1 nm. At each wavelength, we measure the deposition matrix and computationally construct the broadband deposition matrix $\mathcal{A}$ for a given frequency interval of width $\Delta\omega$ centred at ω_0. Then, we compute the eigenvector of $\mathcal{A}$ with the largest eigenvalue corresponding to the maximum broadband deposition channel. Taking this eigenvector as the input wavefront and multiplying it by $\mathcal{Z}(\omega)$ gives the field distribution in the target region at frequency ω. The spatial integration of field intensity in the target provides the deposited energy as a function of frequency detuning $|\omega - \omega_0|$. The results are shown in Fig. 2 for different bandwidths. In the monochromatic case ($\Delta\omega \approx 0$), the energy deposition eigenchannel is highly sensitive to frequency detuning, decaying quickly as ω deviates from ω_0 (black curve). The full-width at half-maximum gives $\delta\omega \simeq 381$ rad ns^{-1}, corresponding to $\delta\lambda \simeq 0.5$ nm (Supplementary Section I).

In Fig. 2, the red, green and blue curves represent the energy deposited by the maximum eigenvectors of $\mathcal{A}$ with increasing bandwidth $\Delta\omega/\delta\omega = 1.5$, 4.5 and 9.0, respectively. Within the designated frequency range, the energy enhancement remains nearly constant and well above 1. Even for $\Delta\omega/\delta\omega = 9$, the maximum eigenchannel of $\mathcal{A}$ sustains a sixfold energy enhancement over random wavefront illuminations. Beyond $\Delta\omega$, the energy enhancement drops but still remains well above 1 for very large frequency detuning.

We stress that the broadband deposition eigenchannel of the largest eigenvalue provides the global maximum for energy delivery (Supplementary Section II). It fully utilizes long-range spectral correlations for broadband enhancement, compared with a naïve approach of partitioning the controlled input spatial channels over the number of spectral channels M, which leads to ~M times reduction in energy enhancement (Supplementary Section II).

Bandwidth dependence

To further investigate the broadband energy deposition, we calculate the maximum eigenvalue ζ_{max} of $\mathcal{A}(\Delta\omega)$, which gives the largest energy that can be delivered to the target in the bandwidth of $\Delta\omega$. Since the mean eigenvalue $\langle\zeta\rangle$ corresponds to the target energy under random wavefront illuminations, $\zeta_{max}/\langle\zeta\rangle$ is equal to the broadband energy enhancement in the target. Figure 3 shows that $\zeta_{max}/\langle\zeta\rangle$ decays with the normalized bandwidth $\Delta\omega/\delta\omega$ for a 10 × 10 μm² target region centred at depth $z = 30$ μm in the disordered waveguide (purple curve).

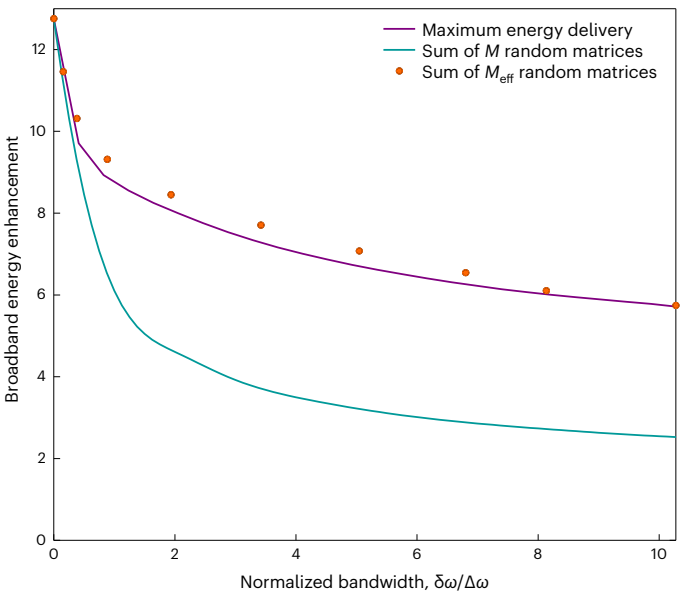

Fig. 3 | Bandwidth dependence of targeted energy delivery. Maximum enhancement of energy within input bandwidth $\Delta\omega$ normalized by $\delta\omega$ at depth $z = 0.6L$, in a 10 × 10 μm² target region centred at depth $z = 30$ μm in the disordered waveguide, is given by the ratio of the largest eigenvalue ζ_{max} of the experimentally measured broadband deposition matrix $\mathcal{A}$ to the mean eigenvalue $\langle\zeta\rangle$ (purple line). Approximating $\mathcal{A}$ by a sum of $M = \Delta\omega/\delta\omega + 1$ random matrices underestimates the energy enhancement (blue line). Reducing M to M_{eff}, to account for long-range spectral correlation, recovers the maximum eigenvalue of $\mathcal{A}$ (red symbols) and agrees with the experimental enhancement.

https://doi.org/10.1038/s41566-024-01446-7

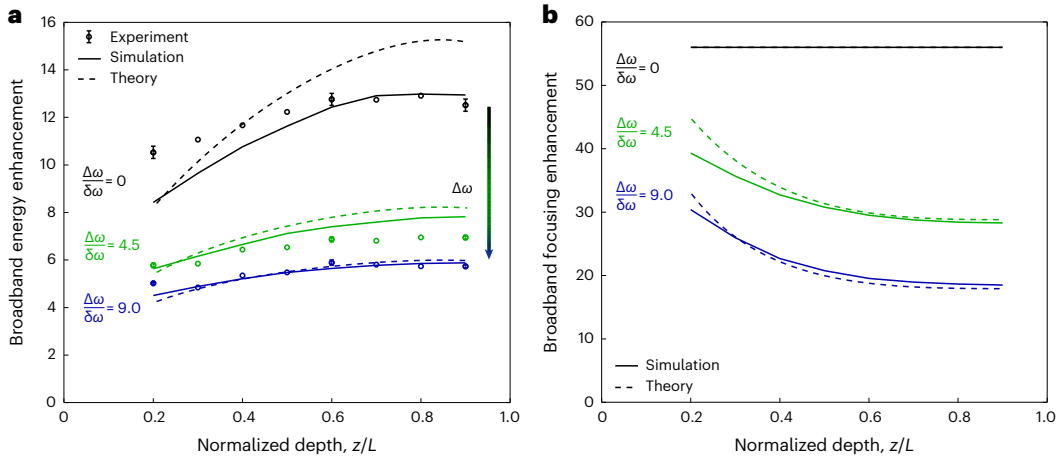

Fig. 4 | Depth dependence of broadband energy delivery. a, Maximum enhancement of energy $\langle\zeta_{max}\rangle/\langle\zeta\rangle$, delivered to a $10 \times 10\ \mu m^2$ target region, as a function of depth z (normalized by the length of disordered waveguide L). Input (normalized) bandwidth $\Delta\omega/\delta\omega$ is fixed to 0 (black), 4.5 (green) and 9.0 (blue), where $\delta\omega$ is the spectral correlation width at depth $z/L = 0.6$. Experimental data (symbols) are compared with numerical results (solid line) and analytical prediction (dashed line). For $\Delta\omega/\delta\omega \gg 1$, the energy enhancement is nearly depth independent. The error bars represent one standard error about the mean with sample size $n = 102\alpha$ (black), $n = 58\alpha$ (green) and $n = 14\alpha$ (blue), respectively, where $\alpha = 0.1\ nm/\delta\lambda \simeq 0.2$ accounts for spectral correlations. **b**, Enhancement of broadband focusing to a wavelength-scale target as a function of normalized depth z/L, for fixed bandwidths $\Delta\omega/\delta\omega$ of 0 (black), 4.5 (green) and 9.0 (blue). When $\Delta\omega/\delta\omega \ll 1$, focusing enhancement is independent of depth, and determined by the degree of control over the input wavefront, which is equal to the number of waveguide modes $N = 55$. As $\Delta\omega/\delta\omega$ increases, the focusing enhancement decays with the depth for $z < L/2$.

To capture the impact of spectral correlations on the scaling of energy enhancement with bandwidth, we model $\mathcal{A}$ in equation (1) as a sum of M_{eff} uncorrelated matrices $\mathcal{A} \simeq \tilde{\mathcal{A}}$, where

$$\tilde{\mathcal{A}} = \frac{1}{M_{eff}} \sum_{m=1}^{M_{eff}} \tilde{\mathcal{Z}}_m^{\dagger} \tilde{\mathcal{Z}}_m. \tag{2}$$

Each random matrix $\tilde{\mathcal{Z}}_m$ represents an independent spectral channel, numerically generated with the same eigenvalue statistics as the measured $\mathcal{Z}(\omega)$ (Supplementary Section III). We plot the energy enhancement of the maximum eigenvector of $\tilde{\mathcal{A}}$ in Fig. 3 for $M_{eff} = M = \Delta\omega/\delta\omega + 1$ (cyan curve). The result is notably smaller than the experimental one (purple curve). For a bandwidth of $\Delta\omega/\delta\omega = 10$, the actual energy enhancement is more than twice that calculated from the random matrix model.

Such dramatic discrepancy results from the lack of correlations between the M random matrices $\tilde{\mathcal{Z}}_m$ used to generate $\tilde{\mathcal{A}}$. Correlations between matrices $\mathcal{Z}(\omega)$ in $\mathcal{A}$ originate from long-range spectral correlations of multiply scattered waves in a diffusive system[52,53]. To account for this, we rescale the number of independent spectral channels M within $\Delta\omega$ to $M_{eff} < M$ (refs. 16,46).

M_{eff} is explicitly determined by the long-range spectral correlation function $C_2(z, |\omega_1 - \omega_2|)$ at depth z (ref. 46):

$$\frac{1}{M_{eff}} = \frac{\bar{C}_2(z, \Delta\omega)}{\bar{C}_2(z, 0)}, \tag{3}$$

where $\bar{C}_2(z, \Delta\omega) = \iint_{\Delta\omega} d\omega_1 d\omega_2 C_2(z, |\omega_1 - \omega_2|)/\Delta\omega^2$. In Supplementary Section IV, we present an analytic expression for $C_2(z, |\omega_1 - \omega_2|)$, thereby providing an explicit equation to compute M_{eff}. Using this expression without any free parameter, we obtain the enhancement (Fig. 3, circles) and recover the experimental result for broadband enhancement to a remarkable degree. Such agreement confirms the importance of long-range spectral correlations for delivering energy over large bandwidths. In the broadband limit $\Delta\omega \gg \delta\omega$, we find $M_{eff} \propto \sqrt{\Delta\omega/\delta\omega(z)} \simeq \sqrt{M}$ (Supplementary Section IV). The reduced number of independent channels ($M_{eff} \ll M$) enables a much greater improvement in the maximum energy deposition using a single wavefront than expected for M uncorrelated channels.

Depth dependence of energy deposition

In the previous section, the depth of the target is fixed. The depth dependence of energy deposition is of great importance for accessing deep inside scattering media. Here we vary the depth z while fixing the input bandwidth $\Delta\omega$. From the experimental data, we plot the maximum eigenvalue of $\mathcal{A}$ versus z for $\Delta\omega/\delta\omega = 0$, 4.5 and 9.0 (Fig. 4a). Surprisingly, the energy enhancement increases with z, and the depth dependence nearly vanishes when $\Delta\omega \gg \delta\omega$. To confirm the experimental results, we conduct numerical simulations using Kwant, a Python package for wave-transport simulations[54] (Methods provides additional details). The simulation results (Fig. 4a, solid lines) have good agreement with the experimental data (symbols), especially at large $\Delta\omega$.

To explain the depth dependence, we analytically compute the broadband energy deposition using filtered random matrix theory[46,55]. A complete derivation (Supplementary Sections III and IV) reveals that for extended-area deposition in the broadband limit, the energy enhancement depends only on $\bar{C}_2(z, \Delta\omega)$:

$$\frac{\langle\zeta_{max}\rangle}{\langle\zeta\rangle} \simeq \gamma + 3\left(\frac{\pi}{2}\right)^{2/3} \gamma^{1/3} - 2, \tag{4}$$

where $\gamma = 3N\bar{C}_2(z, \Delta\omega)/2$. The theoretical predictions (Fig. 4a, dashed lines) match the experimental and numerical results, particularly predicting that the depth dependence nearly vanishes at a large bandwidth. In the limit of $\Delta\omega \gg \delta\omega$, we prove that $\gamma \simeq (16/\pi) L_{\Delta\omega}/\ell_t$, where the coherence length $L_{\Delta\omega} = \sqrt{D/2\Delta\omega} = \sqrt{D\tau_c/2}$ is equal to the diffusion distance that broadband light travels over the coherence time τ_c and D is the diffusion coefficient.

The coherence length sets the range in which long-range correlations can build up, as the latter arise from the crossing of broadband diffusive paths. In the monochromatic limit where $L_{\Delta\omega} \gg L$, long-range correlations can be generated anywhere in the sample, so their weight and energy enhancement increase with the deposition depth. In the opposite broadband limit, they are generated in a layer of thickness $L_{\Delta\omega}$, beyond which their weight saturates and $\langle\zeta_{max}\rangle/\langle\zeta\rangle$ becomes independent of the depth z.

The depth dependence stands in sharp contrast to broadband focusing to a single speckle of wavelength scale. Figure 4b shows the focusing

https://doi.org/10.1038/s41566-024-01446-7

enhancement (ratio of maximum energy within the focal spot over the mean value), obtained from numerical simulations, for different input bandwidths. As $\Delta\omega$ increases, the depth dependence becomes more pronounced. For $\Delta\omega/\delta\omega = 9$, the focusing enhancement rapidly decays with the normalized depth z/L. Such a variation originates from the fact that the broadband focusing is determined by the short-range correlation function $C_1(z, |\omega_1 - \omega_2|)$, which has a distinct depth dependence from $C_2(z, |\omega_1 - \omega_2|)$. In Supplementary Section V, we analytically compute the focusing enhancement from the expression of $C_1(z, |\omega_1 - \omega_2|)$. In Fig. 4b, the analytical results (dashed line) agree well with the numerical results (solid line). In the limit of thick samples ($L \gg L_{\Delta\omega}, z$), the focusing enhancement to a single speckle reduces to $N\bar{C}_1(z, \Delta\omega) \simeq N(2L_{\Delta\omega}/z)^2$.

In general, the energy enhancement for any target size and depth is determined by $\bar{C}_1(z, \Delta\omega)/N_s + \bar{C}_2(z, \Delta\omega)$ where N_s is the number of speckle grains in the target region. The transition from short- to long-range correlation dominance occurs at a critical target size $N_s = \bar{C}_1(z, \Delta\omega)/\bar{C}_2(z, \Delta\omega)$ below (above) which the energy enhancement decreases (increases) monotonically with depth (Supplementary Section VI).

Effect of dissipation

Finally, we investigate how dissipation affects broadband energy delivery. In our experiment, energy loss due to out-of-plane scattering can be described by a diffusive dissipation length $\xi_a = \sqrt{\ell_t \ell_a/2} = 28\ \mu m$, where ℓ_a is the ballistic dissipation length[56]. Since $L \gtrsim \xi_a$, the dissipation is not negligible. The dissipation time $\tau_a = \ell_a/v$ is comparable with the diffusion dwell time of light at the output of the waveguide, $\tau_d = L^2/\pi^2 D$. To compare a system with dissipation to one without dissipation, we conduct numerical simulations where dissipation can be switched off.

In Fig. 5, we plot the numerical results of energy enhancement with and without dissipation as a function of input bandwidth $\Delta\omega$ for a $10 \times 10\ \mu m^2$ target at depth $z = 0.6L$. For monochromatic light, dissipation lowers the energy enhancement, in accordance with the previously demonstrated reduction in transmission enhancement in the presence of weak and moderate dissipation[50]. As $\Delta\omega$ increases, however, the broadband energy enhancement with dissipation approaches that without dissipation. For confirmation, we calculate the energy enhancement from random matrices by rescaling the number of independent spectral channels by M_{eff}. Regardless of absorption, M_{eff} calculated from C_2 gives the energy enhancement in good agreement with the numerical results (Fig. 5).

The convergence of enhancement with and without absorption at large bandwidths indicates that dissipation has little impact on the maximum energy delivery achievable by wavefront shaping. We find that this is because the long-range correlation C_2 loses its dependence on ξ_a in the broadband limit. A physical explanation is given in terms of the coherence time of light $\tau_c = 1/\Delta\omega$. For narrowband input ($\tau_c \gg \tau_a$), dissipation weakens the interference effect responsible for C_2 by attenuating the scattered waves of long paths. More precisely, it reduces the probability of two diffusive paths crossing inside the sample—an effect at the origin of C_2 correlations. The energy enhancement induced by this constructive interference is, therefore, reduced. As $\Delta\omega$ increases, τ_c becomes shorter. Once $\tau_c < \tau_a$, the interference effect is limited by decoherence rather than dissipation: the exchange of field partners occurs inside a volume of thickness $L_{\Delta\omega} < \xi_a$, and the C_2 contribution saturates to $\bar{C}_2(z, \Delta\omega) \simeq (32/3\pi N)L_{\Delta\omega}/\ell_t$. Consequently, the dependence of energy enhancement on dissipation vanishes. This result also contrasts sharply with what is obtained for broadband focusing, which preserves a non-negligible dissipation dependence even in the $\tau_c < \tau_a$ regime (Supplementary Section V).

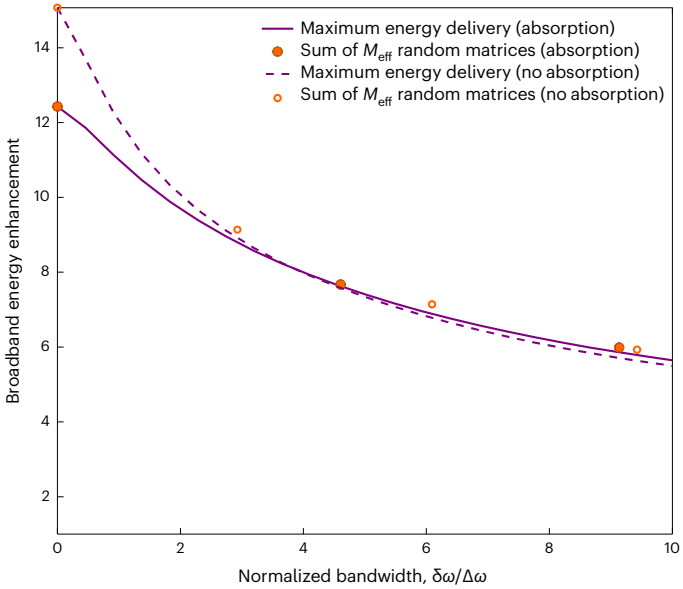

Fig. 5 | Effect of dissipation on energy delivery. Comparison of numerical results with (solid lines) and without (dashed lines) dissipation for maximum energy enhancement $\langle\zeta_{max}\rangle/\langle\zeta\rangle$, in a $10 \times 10\ \mu m^2$ target region centred at the normalized depth $z = 0.6L$. The diffusive dissipation length $\xi_a = 28\ \mu m$ is equal to the experimental value. For $\Delta\omega/\delta\omega \ll 1$, dissipation lowers the energy enhancement. However, for $\Delta\omega/\delta\omega \gg 1$, the energy enhancement becomes insensitive to dissipation. M_{eff} successfully predicts the energy enhancement from the random matrix model, both with (solid circles) and without (open circles) absorption.

Discussion

We have introduced the broadband deposition matrix $\mathcal{A}$, which identifies a single wavefront that delivers the maximum energy from a broadband source deep into a diffusive system. For a target of size much larger than the wavelength, long-range spatial and spectral correlations enhance the energy delivery. The dependence on target depth and on (uniform) dissipation in the sample vanish in the broadband (fast decoherence) limit. These results contrast those for broadband focusing to a wavelength-scale target, which is dictated by short-range correlations, leading to a quick decay of focusing enhancement with depth. This difference highlights that contributions of long-range correlations to broadband energy deposition will dominate at large depths—a result that is not necessarily true for monochromatic energy delivery.

Although this study is performed on two-dimensional diffusive systems, the general conclusion and theoretical model are applicable to three-dimensional systems (Supplementary Section VII). Although it is very difficult to measure the deposition matrix inside a three-dimensional system[57], our theoretical model can still predict the fundamental limit for broadband energy delivery to a large target located at any depth, proportional to $N\bar{C}_2(z, \Delta\omega)$ at leading order, thereby providing an upper bound with which to constrain wavefront optimization. For open-slab geometries where lateral diffusion of light is important, incomplete channel control[16,19] must be accounted for in the evaluation of $\bar{C}_2(z, \Delta\omega)$. Nevertheless, the maximum eigenvalue of the partial broadband deposition matrix still sets the highest possible energy delivered to a target, and the corresponding eigenvector provides the input wavefront. Our approach may also be applied to systems with tailored disorder or scattering, such as photonic crystals[58]. Finally, our methods and results apply more generally to other types of waves, including acoustic waves, microwaves and electron waves, which possess long-range spatial and temporal correlations. Overcoming the hurdle of fast temporal decoherence of these waves would have implications for practical applications, including deep-tissue imaging[59,60], optogenetic control of neurons[61–64], laser microsurgery[59,65] and photothermal therapy[66] deep inside complex media.

Online content

Any methods, additional references, Nature Portfolio reporting summaries, source data, extended data, supplementary information,

acknowledgements, peer review information; details of author contributions and competing interests; and statements of data and code availability are available at https://doi.org/10.1038/s41566-024-01446-7.

References

1. Mosk, A. P., Lagendijk, A., Lerosey, G. & Fink, M. Controlling waves in space and time for imaging and focusing in complex media. *Nat. Photon.* **6**, 283–292 (2012).
2. Rotter, S. & Gigan, S. Light fields in complex media: mesoscopic scattering meets wave control. *Rev. Mod. Phys.* **89**, 015005 (2017).
3. Cao, H., Mosk, A. P. & Rotter, S. Shaping the propagation of light in complex media. *Nat. Phys.* **18**, 994–1007 (2022).
4. Vellekoop, I. M. & Mosk, A. P. Focusing coherent light through opaque strongly scattering media. *Opt. Lett.* **32**, 2309–2311 (2007).
5. Yaqoob, Z., Psaltis, D., Feld, M. S. & Yang, C. Optical phase conjugation for turbidity suppression in biological samples. *Nat. Photon.* **2**, 110–115 (2008).
6. Vellekoop, I. M., van Putten, E. G., Lagendijk, A. & Mosk, A. P. Demixing light paths inside disordered metamaterials. *Opt. Express* **16**, 67–80 (2008).
7. Xu, X., Liu, H. & Wang, L. V. Time-reversed ultrasonically encoded optical focusing into scattering media. *Nat. Photon.* **5**, 154–157 (2011).
8. Judkewitz, B., Wang, Y. M., Horstmeyer, R., Mathy, A. & Yang, C. Speckle-scale focusing in the diffusive regime with time reversal of variance-encoded light (TROVE). *Nat. Photon.* **7**, 300–305 (2013).
9. Horstmeyer, R., Ruan, H. & Yang, C. Guidestar-assisted wavefront-shaping methods for focusing light into biological tissue. *Nat. Photon.* **9**, 563–571 (2015).
10. Vellekoop, I. M. Feedback-based wavefront shaping. *Opt. Express* **23**, 12189–12206 (2015).
11. Vellekoop, I. M. & Mosk, A. P. Universal optimal transmission of light through disordered materials. *Phys. Rev. Lett.* **101**, 120601 (2008).
12. Popoff, S. M. et al. Measuring the transmission matrix in optics: an approach to the study and control of light propagation in disordered media. *Phys. Rev. Lett.* **104**, 100601 (2010).
13. Choi, W., Mosk, A. P., Park, Q. H. & Choi, W. Transmission eigenchannels in a disordered medium. *Phys. Rev. B* **83**, 134207 (2011).
14. Kim, M. et al. Maximal energy transport through disordered media with the implementation of transmission eigenchannels. *Nat. Photon.* **6**, 581–585 (2012).
15. Yu, H. et al. Measuring large optical transmission matrices of disordered media. *Phys. Rev. Lett.* **111**, 153902 (2013).
16. Popoff, S. M., Goetschy, A., Liew, S. F., Stone, A. D. & Cao, H. Coherent control of total transmission of light through disordered media. *Phys. Rev. Lett.* **112**, 133903 (2014).
17. Gérardin, B., Laurent, J., Derode, A., Prada, C. & Aubry, A. Full transmission and reflection of waves propagating through a maze of disorder. *Phys. Rev. Lett.* **113**, 173901 (2014).
18. Davy, M., Shi, Z., Park, J., Tian, C. & Genack, A. Z. Universal structure of transmission eigenchannels inside opaque media. *Nat. Commun.* **6**, 6893 (2015).
19. Hsu, C. W., Liew, S. F., Goetschy, A., Cao, H. & Stone, A. D. Correlation-enhanced control of wave focusing in disordered media. *Nat. Phys.* **13**, 497–502 (2017).
20. Yılmaz, H., Hsu, C. W., Yamilov, A. & Cao, H. Transverse localization of transmission eigenchannels. *Nat. Photon.* **13**, 352–358 (2019).
21. Bender, N., Yamilov, A., Yılmaz, H. & Cao, H. Fluctuations and correlations of transmission eigenchannels in diffusive media. *Phys. Rev. Lett.* **125**, 165901 (2020).
22. Hsieh, C.-L., Pu, Y., Grange, R. & Psaltis, D. Digital phase conjugation of second harmonic radiation emitted by nanoparticles in turbid media. *Opt. Express* **18**, 12283–12290 (2010).
23. Choi, Y. et al. Measurement of the time-resolved reflection matrix for enhancing light energy delivery into a scattering medium. *Phys. Rev. Lett.* **111**, 243901 (2013).
24. Cheng, X. & Genack, A. Z. Focusing and energy deposition inside random media. *Opt. Lett.* **39**, 6324–6327 (2014).
25. Chaigne, T. et al. Controlling light in scattering media non-invasively using the photoacoustic transmission matrix. *Nat. Photon.* **8**, 58–64 (2014).
26. Liu, Y. et al. Optical focusing deep inside dynamic scattering media with near-infrared time-reversed ultrasonically encoded (true) light. *Nat. Commun.* **6**, 5904 (2015).
27. Sarma, R., Yamilov, A. G., Petrenko, S., Bromberg, Y. & Cao, H. Control of energy density inside a disordered medium by coupling to open or closed channels. *Phys. Rev. Lett.* **117**, 086803 (2016).
28. Badon, A. et al. Smart optical coherence tomography for ultra-deep imaging through highly scattering media. *Sci. Adv.* **2**, e1600370 (2016).
29. Jeong, S. et al. Focusing of light energy inside a scattering medium by controlling the time-gated multiple light scattering. *Nat. Photon.* **12**, 277–283 (2018).
30. Katz, O., Ramaz, F., Gigan, S. & Fink, M. Controlling light in complex media beyond the acoustic diffraction-limit using the acousto-optic transmission matrix. *Nat. Commun.* **10**, 717 (2019).
31. Durand, M., Popoff, S. M., Carminati, R. & Goetschy, A. Optimizing light storage in scattering media with the dwell-time operator. *Phys. Rev. Lett.* **123**, 243901 (2019).
32. Boniface, A., Blochet, B., Dong, J. & Gigan, S. Noninvasive light focusing in scattering media using speckle variance optimization. *Optica* **6**, 1381–1385 (2019).
33. Horodynski, M. et al. Optimal wave fields for micromanipulation in complex scattering environments. *Nat. Photon.* **14**, 149–153 (2020).
34. Yang, J. et al. Focusing light inside live tissue using reversibly switchable bacterial phytochrome as a genetically encoded photochromic guide star. *Sci. Adv.* **5**, eaay1211 (2019).
35. Boniface, A., Dong, J. & Gigan, S. Non-invasive focusing and imaging in scattering media with a fluorescence-based transmission matrix. *Nat. Commun.* **11**, 6154 (2020).
36. Lambert, W., Cobus, L. A., Frappart, T., Fink, M. & Aubry, A. Distortion matrix approach for ultrasound imaging of random scattering media. *Proc. Natl Acad. Sci. USA* **117**, 14645–14656 (2020).
37. Badon, A. et al. Distortion matrix concept for deep optical imaging in scattering media. *Sci. Adv.* **6**, eaay7170 (2020).
38. Bouchet, D., Rotter, S. & Mosk, A. P. Maximum information states for coherent scattering measurements. *Nat. Phys.* **17**, 564–568 (2021).
39. Lee, Y.-R. et al. Wave propagation dynamics inside a complex scattering medium by the temporal control of backscattered waves. *Optica* **10**, 569–577 (2023).
40. Bender, N. et al. Depth-targeted energy delivery deep inside scattering media. *Nat. Phys.* **18**, 309–315 (2022).
41. van Beijnum, F., van Putten, E. G., Lagendijk, A. & Mosk, A. P. Frequency bandwidth of light focused through turbid media. *Opt. Lett.* **36**, 373–375 (2011).
42. Paudel, H. P., Stockbridge, C., Mertz, J. & Bifano, T. Focusing polychromatic light through strongly scattering media. *Opt. Express* **21**, 17299–17308 (2013).

43. Andreoli, D. et al. Deterministic control of broadband light through a multiply scattering medium via the multispectral transmission matrix. *Sci. Rep.* **5**, 10347 (2015).
44. Mounaix, M. et al. Spatiotemporal coherent control of light through a multiple scattering medium with the multispectral transmission matrix. *Phys. Rev. Lett.* **116**, 253901 (2016).
45. Mounaix, M., de Aguiar, H. B. & Gigan, S. Temporal recompression through a scattering medium via a broadband transmission matrix. *Optica* **4**, 1289–1292 (2017).
46. Hsu, C. W., Goetschy, A., Bromberg, Y., Stone, A. D. & Cao, H. Broadband coherent enhancement of transmission and absorption in disordered media. *Phys. Rev. Lett.* **115**, 223901 (2015).
47. Liew, S. F., Popoff, S. M., Mosk, A. P., Vos, W. L. & Cao, H. Transmission channels for light in absorbing random media: from diffusive to ballistic-like transport. *Phys. Rev. B* **89**, 224202 (2014).
48. Liew, S. F. & Cao, H. Modification of light transmission channels by inhomogeneous absorption in random media. *Opt. Express* **23**, 11043–11053 (2015).
49. Sarma, R., Yamilov, A., Liew, S. F., Guy, M. & Cao, H. Control of mesoscopic transport by modifying transmission channels in opaque media. *Phys. Rev. B* **92**, 214206 (2015).
50. Yamilov, A., Petrenko, S., Sarma, R. & Cao, H. Shape dependence of transmission, reflection, and absorption eigenvalue densities in disordered waveguides with dissipation. *Phys. Rev. B* **93**, 100201 (2016).
51. Sarma, R., Yamilov, A., Neupane, P. & Cao, H. Using geometry to manipulate long-range correlation of light inside disordered media. *Phys. Rev. B* **92**, 180203 (2015).
52. Stephen, M. J. & Cwilich, G. Intensity correlation functions and fluctuations in light scattered from a random medium. *Phys. Rev. Lett.* **59**, 285 (1987).
53. Berkovits, R. & Feng, S. Correlations in coherent multiple scattering. *Phys. Rep.* **238**, 135–172 (1994).
54. Groth, C. W., Wimmer, M., Akhmerov, A. R. & Waintal, X. Kwant: a software package for quantum transport. *New J. Phys.* **16**, 063065 (2014).
55. Goetschy, A. & Stone, A. D. Filtering random matrices: the effect of incomplete channel control in multiple scattering. *Phys. Rev. Lett.* **111**, 063901 (2013).
56. Yamilov, A. G. et al. Position-dependent diffusion of light in disordered waveguides. *Phys. Rev. Lett.* **112**, 023904 (2014).
57. Hong, P., Ojambati, O. S., Lagendijk, A., Mosk, A. P. & Vos, W. L. Three-dimensional spatially resolved optical energy density enhanced by wavefront shaping. *Optica* **5**, 844–849 (2018).
58. Uppu, R., Adhikary, M., Harteveld, C. A. & Vos, W. L. Spatially shaping waves to penetrate deep inside a forbidden gap. *Phys. Rev. Lett.* **126**, 177402 (2021).
59. Yu, H. et al. Recent advances in wavefront shaping techniques for biomedical applications. *Curr. Appl. Phys.* **15**, 632–641 (2015).
60. Yoon, S. et al. Deep optical imaging within complex scattering media. *Nat. Rev. Phys.* **2**, 141–158 (2020).
61. Fenno, L., Yizhar, O. & Deisseroth, K. The development and application of optogenetics. *Annu. Rev. Neurosci.* **34**, 389–412 (2011).
62. Yoon, J. et al. Optogenetic control of cell signaling pathway through scattering skull using wavefront shaping. *Sci. Rep.* **5**, 13289 (2015).
63. Pégard, N. C. et al. Three-dimensional scanless holographic optogenetics with temporal focusing (3D-SHOT). *Nat. Commun.* **8**, 1228 (2017).
64. Ruan, H. et al. Deep tissue optical focusing and optogenetic modulation with time-reversed ultrasonically encoded light. *Sci. Adv.* **3**, eaao5520 (2017).
65. Yanik, M. F. et al. Neurosurgery: functional regeneration after laser axotomy. *Nature* **432**, 822 (2004).
66. Pernot, M. et al. In vivo transcranial brain surgery with an ultrasonic time reversal mirror. *J. Neurosurg.* **106**, 1061–1066 (2007).

Methods

Sample fabrication

The waveguiding structures used in our experiment are fabricated on a silicon-on-insulator wafer using a combination of electron-beam lithography and reactive ion etching[40,67]. Each structure consists of four sections: a ridge waveguide with a width of 300 μm and a length of 15 mm, an adiabatic taper (15° angle) where the waveguide width gradually decreases from 300 to 15 μm, a weak-scattering buffer region with a width of 15 μm and a length of 25 μm, and a strong-scattering region with a width of 15 μm and a length of 50 μm. The last two segments have randomly distributed air holes with a diameter of 100 nm, and air-filling fractions of 0.55% and 5.50%, respectively. Both regions support 55 spatial modes around the wavelength λ = 1,550 nm. Light is confined by a photonic-crystal triangle-lattice boundary in the last three sections of the structure. The photonic-crystal boundary consists of 16 layers of air holes with a radius of 155 nm and a lattice constant of 440 nm. The boundary provides a complete two-dimensional photonic bandgap for transverse-electric-polarized light of wavelength ranging from 1,120 to 1,580 nm. The tapered and buffer regions facilitate mode mixing and excitation of high-order modes in the waveguide[27].

The relevant parameters for light transport in the disordered waveguides are the transport mean free path ℓ_t and diffusive dissipation length ξ_a. Their values are extracted from fitting the mean and variance of experimentally measured cross-section-averaged intensity with numerical results, as detailed in the supplementary information of ref. 51. In the buffer region, ℓ_t = 33.0 μm and ξ_a = 280.0 μm, whereas in the strong-scattering region, ℓ_t = 3.3 μm and ξ_a = 28.0 μm (refs. 40,67).

Optical setup

A detailed schematic of our experimental setup is provided elsewhere[40,67]. The monochromatic light (linewidth, 100 kHz) from a wavelength-tunable laser (Keysight 81960A) is split into two beams. One beam is modulated by a phase-only SLM (Hamamatsu LCOS X10468) and then injected into one of the waveguides via the edge of the wafer. The other beam is used as a reference beam that is spatially overlapped with the out-of-plane scattered light from the diffusive waveguide. A charge-coupled device camera (Allied Vision Goldeye G-032 Cool) records the resulting interference pattern, from which the complex field profile across the diffusive waveguide is obtained.

Deposition matrix measurement

The deposition matrix relates an orthonormal set of input wavefronts to the corresponding spatial field distributions within the target region[40]. By sequentially applying an orthogonal set of one-dimensional phase patterns to the 128 SLM macropixels and measuring the field within the sample, we acquire a matrix that maps the field from the SLM to the field inside the disordered waveguide $\mathcal{Z}_{\mathrm{slm}\to\mathrm{int}}$. This matrix encompasses information about both light transport inside the waveguide and light propagation from the SLM to the waveguide. To separate these, we add an auxiliary weakly scattering region in front of the diffusive region called the 'buffer' region. We recover the field right in front of the strongly scattering region by imaging the light scattered out of plane from the buffer. The length of the buffer region is 25 μm, which is shorter than its 32-μm-length transport mean free path. As a result, light only experiences single scattering in the buffer; therefore, the diffusive wave transport in the original disordered region is not appreciably altered.

With access to the field inside the buffer, we can construct the matrix relating the field on the SLM to the buffer, $\mathcal{Z}_{\mathrm{slm}\to\mathrm{buff}}$. From $\mathcal{Z}_{\mathrm{slm}\to\mathrm{int}}$, we can also construct the deposition matrix to a selected target region, $\mathcal{Z}_{\mathrm{slm}\to\mathrm{tar}}$, which maps the field from the SLM to a region inside the diffusive waveguide. With these, we calculate the matrix that maps the field from the buffer to the target, $\mathcal{Z}_{\mathrm{buff}\to\mathrm{tar}} = \mathcal{Z}_{\mathrm{slm}\to\mathrm{tar}}\,\mathcal{Z}^{-1}_{\mathrm{slm}\to\mathrm{buff}}$, using Moore–Penrose matrix inversion. We keep only the top N = 55 singular vectors with large singular values (N is the number of waveguide modes), to suppress the experimental noise that primarily lies in the singular vectors with small singular values. This procedure is repeated for 50 wavelengths in the 1,551.0–1,556.0 nm range with a step size of 0.1 nm, to obtain the frequency-resolved deposition matrix $\mathcal{Z}_{\mathrm{buff}\to\mathrm{tar}}(\omega)$.

In the sequential measurement of $\mathcal{Z}_{\mathrm{buff}\to\mathrm{tar}}(\omega)$, the N = 55 dimensional subspace kept in the matrix inversion will not be the same for all the measured frequencies due to both experimental noise and waveguide dispersion, making it very difficult to construct the broadband deposition matrix $\mathcal{A}_{\mathrm{buff}\to\mathrm{tar}}(\Delta\omega)$. To obtain a common subspace of all the frequencies, we calculate the extrinsic mean for vector subspaces defined as the average of the projection matrices for each subspace[68]. This is valid as long as dispersion is relatively weak inside the buffer. When we perform the Moore–Penrose pseudo-inverse for the deposition matrix for each frequency, we project onto the extrinsic subspace mean such that all the deposition matrices share the same N-dimensional space in the buffer region. This procedure allows us to not only build the broadband deposition matrix but also to compute the field distribution at frequency ω_2 for the input wavefront given by the deposition eigenchannel at ω_1.

The broadband matrix $\mathcal{A}$ is constructed with constant intensity $I(\omega)$ within $\Delta\omega$. The average intensity in the target region is recorded during the experiment before matrix inversion. It is integrated both spatially and spectrally to give the broadband energy within the target region under random wavefront illumination.

We measure the deposition matrices in two disorder realizations. The effective number of uncorrelated realizations is further increased by scanning the probed wavelength over the 1,551–1,556 nm range. For each disorder realization, we perform 51 measurements at wavelengths separated by 0.1 nm. With a correlation width of 0.5 nm, effectively ten uncorrelated realizations are obtained for each disordered waveguide.

Numerical simulations

We perform numerical simulations of wave propagation in planar waveguides using Kwant[54,56]. The simulated waveguides have the same dimensions and parameters as in the experiment: width W, length L, refractive index and number of waveguide modes N. The transport mean free path ℓ_t = 3.3 μm and the diffusive dissipation length ξ_a = 28 μm are identical to the experimental values. In the numerical simulations, we can turn off the dissipation by setting $\xi_a = \infty$. To be consistent with our experiment, the deposition matrices map the fields from a buffer region to 10 × 10 μm^2 target regions at varying depths. All the numerical results are averaged over 200 disorder realizations.

Data availability

Source data are provided with this paper. All other data supporting the findings in this study are available from the corresponding author upon reasonable request.

References

67. Bender, N. et al. Coherent enhancement of optical remission in diffusive media. *Proc. Natl Acad. Sci. USA* **119**, e2207089119 (2022).
68. Srivastava, A. & Klassen, E. Monte Carlo extrinsic estimators of manifold-valued parameters. *IEEE Trans. Signal Process.* **50**, 299–308 (2002).

Acknowledgements

We thank C.-W. Chen, K. Kim, S. Han, L. Shaughnessy, P. Miao, S. Halladay and Z. Lai for valuable discussions. This work is supported partly by the National Science Foundation (NSF) under grant nos. DMR-1905465 (R.M. and H.C.) and no. DMR-1905442 (A.Y.) and the Office of Naval Research (ONR) under grant no. N00014-221-1-2026

(H.C.). It has also received support under the program Investissements d'Avenir launched by the French Government (A.G.).

Author contributions

R.M. and N.B. performed the experiments. R.M. analysed the data. N.B. fabricated the samples. A.G. developed the analytic theory. C.W.H. contributed to the theoretical analysis. H.Y. contributed to the experimental analysis. R.M. and A.Y. performed the numerical simulations. H.C. initiated the project and supervised the research. All authors contributed to the interpretation of the results. R.M. and A.G. prepared the paper, H.C. edited it and all authors provided feedback.

Competing interests

The authors declare no competing interests.

Additional information

Supplementary information The online version contains supplementary material available at https://doi.org/10.1038/s41566-024-01446-7.

Correspondence and requests for materials should be addressed to Hui Cao.

Peer review information *Nature Photonics* thanks Jacopo Bertolotti, Roarke Horstmeyer and the other, anonymous, reviewer(s) for their contribution to the peer review of this work.